Supplementary for Metasurface-Enabled Small-Satellite Polarisation Imaging

Sarah E. Dean[a,*], Neuton Li[a], Josephine Munro[a],
Robert Sharp[b], Dragomir N. Neshev[a], and Andrey A. Sukhorukov[a]
[a] *ARC Centre of Excellence for Transformative Meta-Optical Systems (TMOS), Department of Electronic Materials Engineering, Research School of Physics, Australian National University, Canberra, ACT 2600, Australia.*
[b] *Research School of Astronomy and Astrophysics, Australian National University, Weston Creek, ACT 2611, Australia.*

[*]Corresponding Author. Email: sarah.dean@anu.edu.au

This PDF file includes:
Sections S1 to S4
Figures S1 to S12

Contents

S1 Estimated achievable resolution

Here, we present the Fourier analysis of our metasurface to give an order-of-magnitude estimate of the achievable resolution of imaging. It is important to match the achievable theoretical resolution limit with the resolution requirements of the intended remote Earth observation application. This ensures the polarimetric resolution is matched with the imaging resolution of the system, allowing for the maximum amount of useful information to be collected. The estimate uses the image sampling illustrated in figure S1(a), and the scaling regions indicated on the simple imaging system in S1(b).

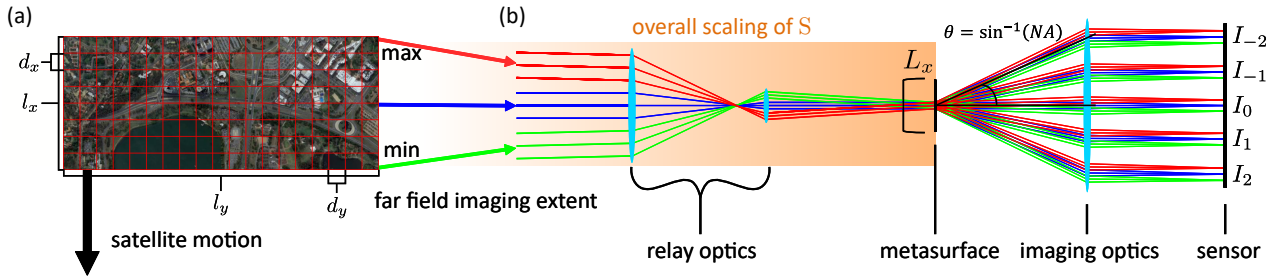

Figure S1: (a) An example of the image sampling of a target imaging area, where each grid square corresponds to one point of polarimetric image data at the sensor. l_x, l_y are the on-ground dimensions of the target, and d_x, d_y on-ground dimensions of a sample (b) Illustration of the simplest imaging system that could be used within the satellite system. The orange area indicates the optics and beam propagation encompassed by the S scaling factor.

To sufficiently image the reflected polarimetric information from the Earth's surface, the metasurface needs to have an overall area and periodicity that matches the desired sampling rate of the satellite's imaging swath.

As the imaging target is in the far field from the metasurface, the Fourier image of the Earth's surface (target plane) reaches the metasurface. Therefore, the smallest resolvable element size

in the target plane, d_x, is inversely proportional to the size (diameter) of the metasurface in the x direction, L_x. A simple scaling factor, ε, is introduced to account for the magnification of the front-end satellite optics. And so, the size of the metasurface needs to meet the resolution requirement of:

$$L_x > \frac{\varepsilon}{d_x}. \tag{S1}$$

To sufficiently sample the full field of view of the swath, a single period of the metasurface p_x must be smaller than the smallest component of the Fourier image reaching the metasurface. The smallest component of the Fourier image in the x direction is $\frac{\varepsilon}{l_x}$, with l_x being the on-ground size of the swath in the x direction. And so, the periodicity size of the metasurface needs to also meet the field of view requirement of:

$$p_x > \frac{\varepsilon}{l_x}. \tag{S2}$$

Dividing Eq. (S1) by (S2) gives a relationship between periodicity in the metasurface and the sampling rate of the target plane:

$$\frac{L_x}{p_x} > \frac{l_x}{d_x}. \tag{S3}$$

The diffraction angles of the polarisation measurements and half of the angular width of the Fourier image at the metasurface determine the minimum numerical aperture to capture all measurements. For 5 diffraction orders in the x-direction giving a maximum diffraction angle of $\sin^{-1}(2\lambda/p_x)$, the minimum numerical apertures in the x- and y- directions are given by:

$$\begin{aligned} \mathrm{NA}_x &= \frac{2\lambda}{p_x} + \sin(\theta_{x2}), \\ \mathrm{NA}_y &= \sin(\theta_{y2}), \end{aligned} \tag{S4}$$

with θ_x and θ_y the half angular widths of the image. Assuming spherical optics so that $NA_x = NA_y$, and that the x-direction half angle of the metasurface is much smaller than the ± 2 diffraction angles, the overall minimum numerical aperture can be approximated as:

$$\mathrm{NA} = \frac{2\lambda}{p_x}. \tag{S5}$$

The NA can be rearranged to give:

$$p_x = \frac{2\lambda}{\mathrm{NA}}, \tag{S6}$$

which can be substituted into equation (S3) to give:

$$\frac{L_x \mathrm{NA}}{2\lambda} > \frac{l_x}{d_x}. \tag{S7}$$

This gives the achievable x-direction image sampling for a particular imaging lens NA and the size of the metasurface in the x-direction. Finally, as $NA_x = NA_y$ for the assumed spherical optics, the equivalent equality for the y-direction is simply:

$$\frac{L_y \mathrm{NA}}{2\lambda} > \frac{l_y}{d_y}. \tag{S8}$$

Multiplying equations (S7) and (S8) together gives the total number of image samples $\frac{l_x l_y}{d_x d_y}$ for imaging optics with a specific NA and the overall metasurface area:

$$\frac{L_x L_y \mathrm{NA}^2}{4\lambda^2} > \frac{l_x l_y}{d_x d_y}. \tag{S9}$$

This demonstrates that a sufficient polarisation imaging resolution may be achieved regardless of the diffraction angle of the intensity measurements by increasing the overall area of the fabricated metasurface.

There are a few considerations for choosing the NA of the diffracted measurements. Smaller NAs result in much more forward diffraction angles, which is beneficial for the scaling and placement of the images on the camera sensor. However, smaller NAs pose issues for optimisation times and transmission efficiencies due to corresponding to larger design periods with more diffraction orders to suppress.

S2 Wavelength and angular robustness of design

The metasurface design was simulated at different incident angles and wavelengths to evaluate the polarimetric performance under imaging conditions. Performance is maintained for an imaging swath of 20° [Figure S2(a)] by 8° [Figure S2(b)], resulting in a large useable field-of-view for imaging. We also identify an operating wavelength range of 842-852 nm with high polarimetric performance [Figure S2(c)].

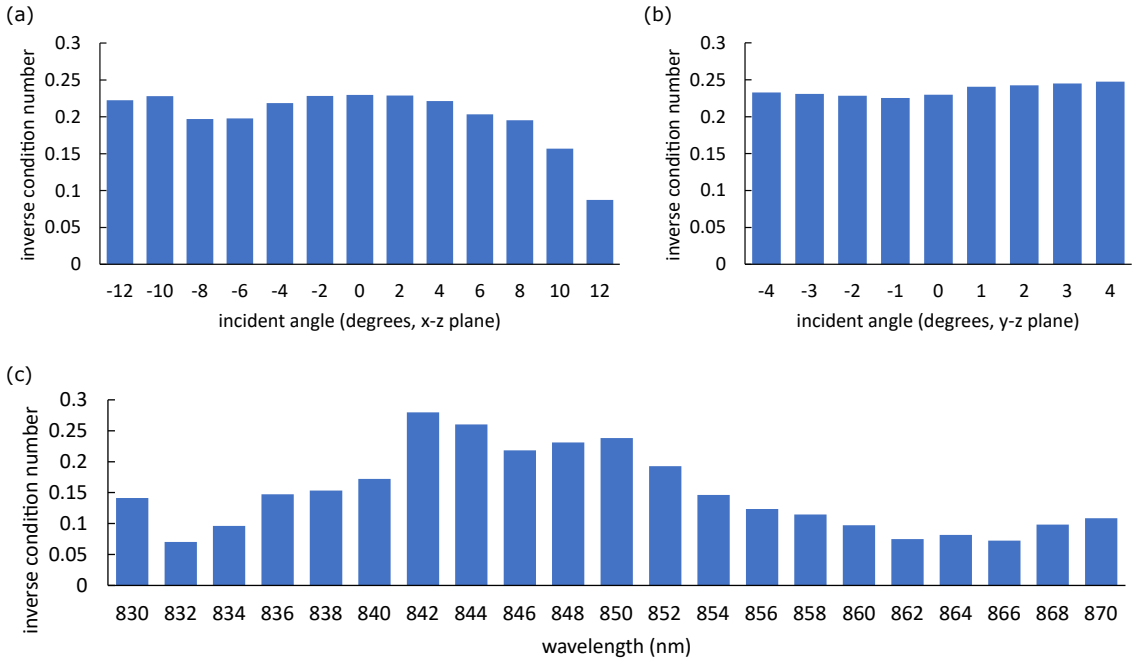

Figure S2: Inverse condition number under various incident light parameters; (a) incident angle in the x-z plane, (b) incident angle in the y-z plane, (c) incident wavelength.

S3 Effect of absorption of silicon on the performance of the metasurface

At a wavelength of 850 nm, crystalline silicon has a complex refractive index of $n + ik = 3.65 + i0.00394$ [S1]. The imaginary component of the refractive index is small, and the thickness

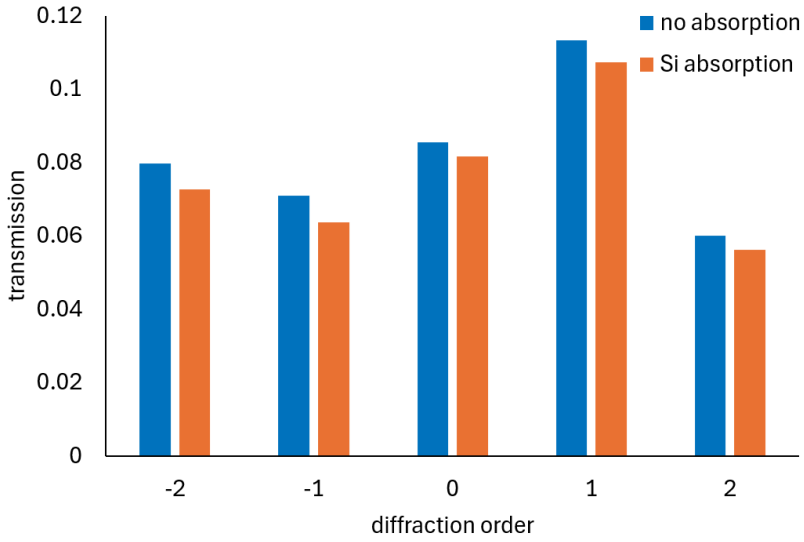

Figure S3: Unpolarised transmission of incident light at the 850 nm wavelength to different output diffraction orders for the metasurface simulated without absorption (blue) and with the absorption of crystalline silicon (orange).

of the silicon layer in the metasurface is 1 μm, resulting in only 3% of total transmission losses stemming from the absorption of silicon, see Figure S3. The polarisation reconstruction performance is only slightly impacted by the absorption, as the inverse condition number of the metasurface instrument matrix without absorption is 0.24, and with absorption is 0.23.

S4 Preliminary Experimental Results

S4.1 Metasurface fabrication

The metasurface was fabricated using electron beam lithography at the Melbourne Centre for Nanofabrication (MCN) in the Victorian Node of the Australian National Fabrication Facility (ANFF). Multiple samples were fabricated, with the scanning electron microscope images of the best performing metasurface sample shown in Figure S4. The overall pattern of the metasurface

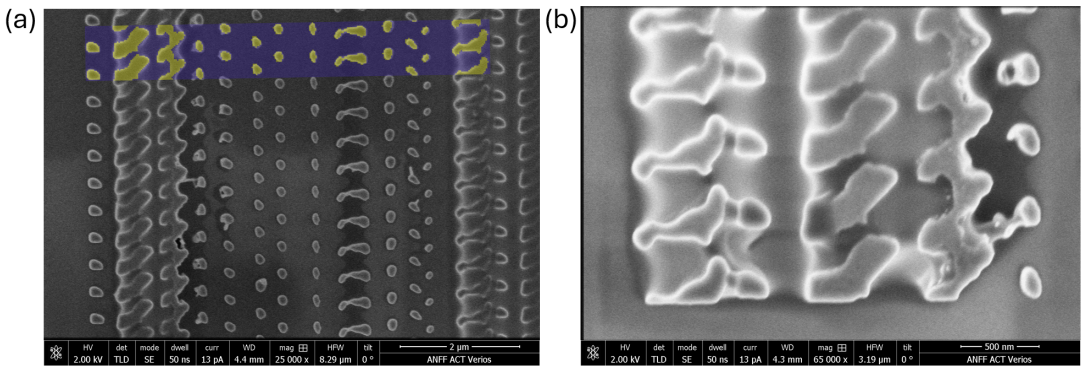

Figure S4: Scanning electron microscope images of the fabricated metasurface. (a) A section of the metasurface, showing similarity between the fabricated structure and the overlaid optimised pattern. (b) Close view of the primary fabrication error, showing an incomplete etch of the pattern. This has an effect on the polarimetric behaviour of the metasurface.

was fabricated accurately and consistently across the metasurface [Figure S4(a)]; however, some areas of the metasurface were not fully etched [Figure S4(b)]. The polarisation reconstruction performance of the metasurface is significantly affected by this fabrication issue, but is still measurable and analysed in the following sections of the supplementary.

S4.2 Experimental characterisation set-up

The experimental set-up for the polarimetric characterisation and analysis of the metasurface is shown in Figure S5. Polarisation states are prepared using the linear polariser, quarter waveplate, and half waveplate, and polarisation measurements are simultaneously captured using an objective with a high numerical aperture (NA). The NA of the objective allows us to capture up to the ±4 diffraction orders for additional analysis of the metasurface polarimetric behaviour. The power fluctuation of the laser is constantly monitored, which we found was required for calibration of the results.

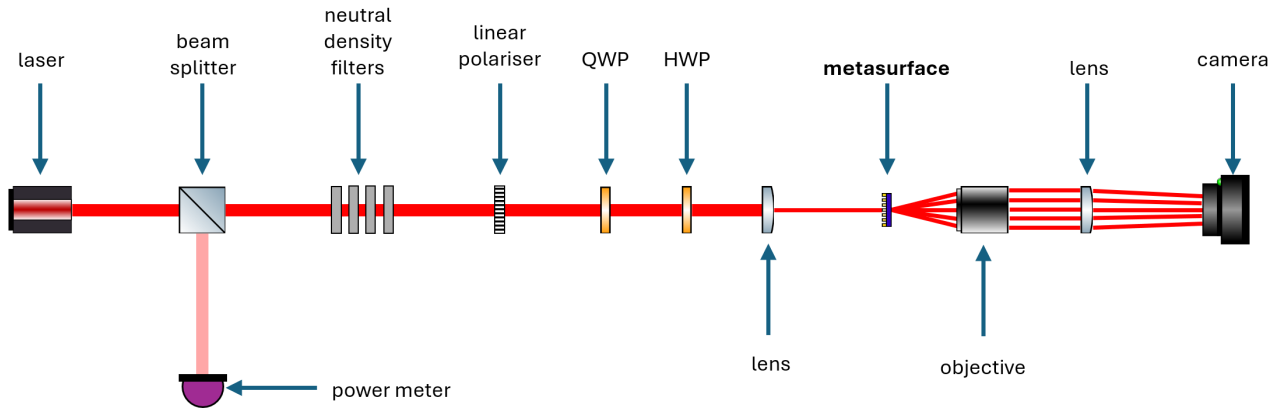

Figure S5: Experimental set-up for the polarimetric characterisation of the metasurface.

S4.3 Experimental Polarimetric Behaviour

Due to the fabrication inaccuracies discussed above, the experimental behaviour of our fabricated metasurface does not match the simulated behaviour of the theoretically designed pattern. Figure S6 shows the significant amount of light being diverted into higher orders, +4,+3,-3,-4. The +/- 5 orders, not captured in this picture, also have a significant amount of light diverted to them.

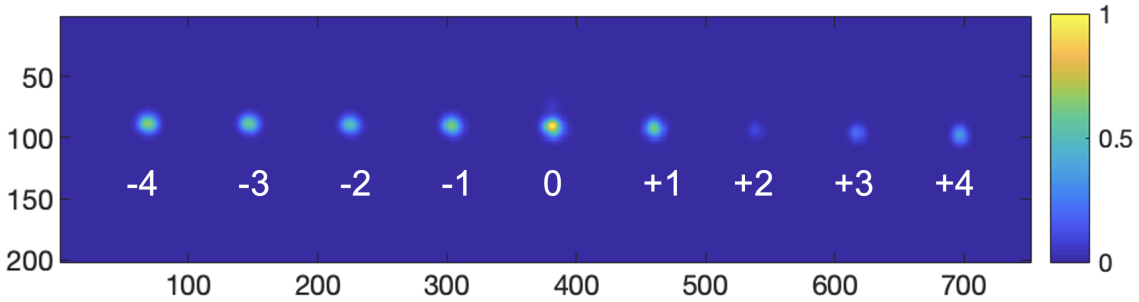

Figure S6: Experimental camera images showing a characteristic output diffraction pattern.

The experimentally determined inverse condition number and analyser orders for all the orders between -4 and +4 inclusive, $\vec{s}_n$, are shown in Figure S7(a), where $\vec{s}_n$ is calculated from

the instrument matrix, and is defined as:

$$\vec{s}_n = \frac{1}{\sqrt{M_{n,1}^2 + M_{n,2}^2 + M_{n,3}^2}} \times [M_{n,1},\ M_{n,2},\ M_{n,3}]; \tag{S10}$$

The inverse condition number of all analysis orders is 0.1354, indicating that the metasurface has polarisation reconstruction capabilities using all nine recorded diffraction orders. For better comparison with the intended usage of the metasurface, we instead consider a set of five measurements from the recorded nine diffraction orders.

The analyser vectors of central five orders are shown in Figure S7(b). The condition number from these set of vectors is 0.0168, indicating that it has poor polarisation reconstruction performance. This is qualitatively supported by how these analysis states span the Poincaré sphere, with the spread of the central five orders from the fabricated metasurface being limited. Alternatively, the orders (-4,-3,-2,+1,+4) shown in Figure S7(c) have an inverse condition number of 0.1535, the highest possible from a combination of five analysis states from Figure S7(a). Despite the polarimetric behaviour deviating from the simulation, the polarimetry performance from the (-4,-3,-2,+1,+4) analysis vectors is sufficient for proof-of-concept analysis of polarimetry and error monitoring.

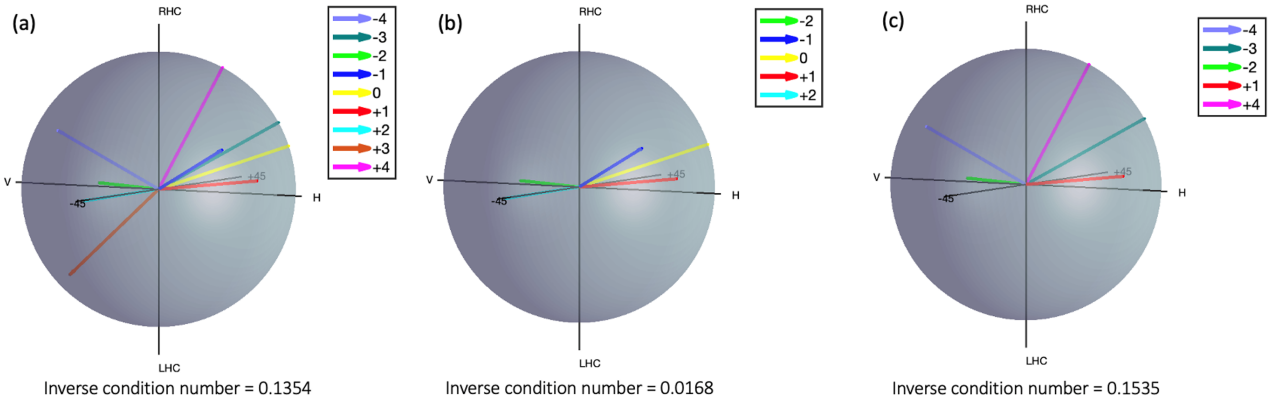

Figure S7: Experimentally determined analyser vectors $\vec{s}_n$ for (a) all orders, (b) central five orders only, (c) selected five orders with the highest polarimetric performance.

The diattenuation and efficiency for each analyser was calculated from the experimental data, and is shown in Figure S8. Diattenuation is defined in the following equation:

$$\text{Diattenuation}_n = \sqrt{\frac{M_{n,1}^2 + M_{n,2}^2 + M_{n,3}^2}{M_{n,0}^2}}, \tag{S11}$$

where 100% represents a perfect polariser. As we are using the maximum likelihood method for polarisation reconstruction, individual diffraction orders do not need to be perfect polarisers to achieve successful polarisation measurements, as discussed in the main paper and in Ref. [S2]. The efficiency is analogous to the unpolarised transmission of light, and is equal to $M_{n,0}$. A perfect polarimeter with five analysers would therefore have efficiencies of 20% in each order. For our metasurface, 37.2% of incident light is diffracted into our measured nine diffraction orders, and 22.0% of incident light directed to our chosen set of five diffraction orders. The deviation of the behaviour of the fabricated metasurface compared to the simulation is likely due to the imperfections in the fabrication process seen in the SEM images [Figure S4].

Further analysis on the polarisation reconstruction and error monitoring behaviour is performed for only our identified highest performing set of five analysis states in the following sections.

S4.4 Calibration Method

Calibration of a polarimeter follows the general procedure of illuminating the instrument with a number of accurately known Stokes states, $\vec{S}_{true}$ (referred to as calibration states) and measuring the power (or intensity) for each of these calibration states. Calibration is crucial for the accuracy of a polarimeter, as it provides an experimental measurement of the analyser vectors, which can deviate from the theoretical values due to manufacturing imperfections.

The accuracy of calibration is often the largest source of error for a polarimeter [S3]. Unlike with a conventional polarimetry systems, where a tetrahedral set of calibration states are the most accurate [S4], we choose to use a random distribution of calibration states to give the most accurate $\vec{S}_{measured}$ reconstructions. This is potentially due to our analysers being partial polarisers, with diattenuation between approximately 20% and 80% [Figure S8(a)], resulting in higher accuracy calibration when using many states spanning the Poincaré sphere.

Our calibration data set consists of 30 random inputs $\vec{S}_{true}$. During our calibration, we also constantly monitor the intensity of the laser source such that we can correct for laser intensity fluctuations. The instrument matrix created from this calibration data set is used to generate the analyser vectors and inverse condition numbers seen in Figure S7. The following analysis will be presented only on the selected high-performing orders (-4,-3,-2,+1,+4), unless otherwise specified.

The accuracy of the calibration can be estimated by comparing the $\vec{S}_{true}$ and the reconstructed $\vec{S}_{measured}$. Figure S9 shows the overlay of $\vec{S}_{true}$ (red crosses) and $\vec{S}_{measured}$ (vectors) on a Poincaré sphere for a selection of eight states from the calibration set, including the measurements with the highest and lowest error. Using $\delta\vec{S} = \vec{S}_{measured} - \vec{S}_{true} = (\delta S_0,\ \delta S_1,\ \delta S_2,\ \delta S_3)$, the root-mean-square error (rms error) is calculated as:

$$\text{rms error} = \sqrt{\frac{1}{4N}\sum_{j=0}^{N}\sum_{i=0}^{3}|\delta S_{i,j}|^2}, \tag{S12}$$

where N is the number of test $\vec{S}$ ($N = 30$ for the calibration). Since we are using calibration frames that are corrected for intensity fluctuation, there is no normalisation needed to compare $\vec{S}_{true}$ and $\vec{S}_{measured}$.

The rms error for the selected orders (-4,-3,-2,+1,+4) is 2.78% in the calibration set. A single number to describe accuracy is more important for comparing many different data sets,

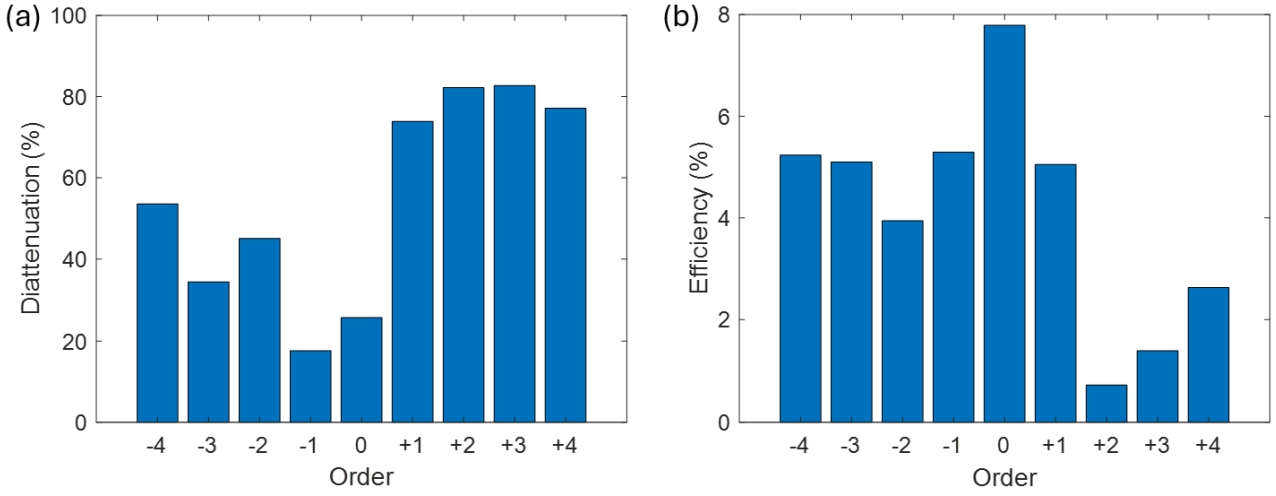

Figure S8: (a) Experimental diattenuation and (b) efficiency for each diffraction order.

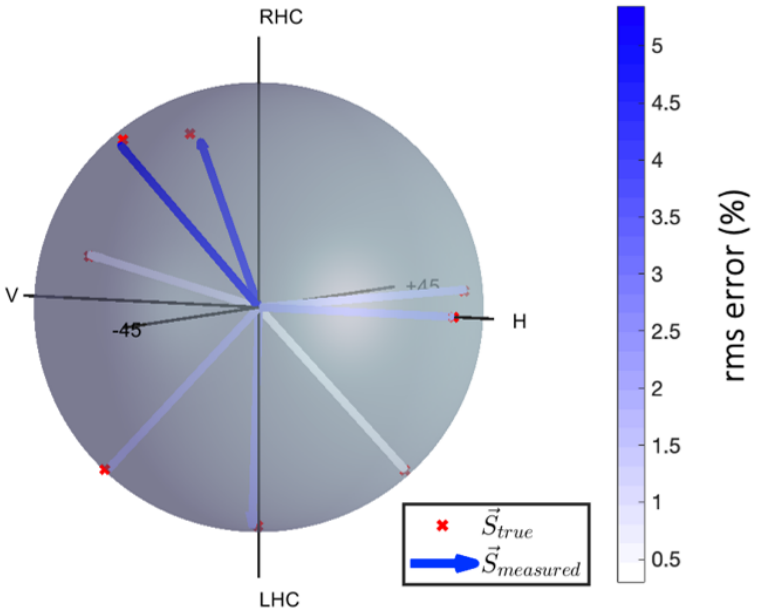

Figure S9: $\vec{S}_{true}$ (red crosses) and $\vec{S}_{measured}$ (vectors) for a selection of 8 states from the set of 30 random calibration states, including the measurements with the highest and lowest error. The rms error between $\vec{S}_{true}$ and $\vec{S}_{measured}$ is given by the colour of the $\vec{S}_{measured}$ vector.

but here we will also present a more thorough analysis of reconstruction error to explain any sources of systematic error. The colour of the $\vec{S}_{measured}$ vectors in Figure S9 shows the rms error for the eight states selected from the calibration set. The $\vec{S}_{measured}$ with the highest rms error is located in the (V, -45, RHC) quadrant. Referring back to the analyser vectors [Figure S7(c)], the -4 analyser vector is the only analyser in the (V, -45, RHC) quadrant, and although it has a reasonably high diattenuation, it comparatively has quite a low efficiency. The distribution of rms error is therefore a complex interaction between the diattenuation, efficiency, and proximity of analyser vectors.

S4.5 Error Monitoring Test

After calibration, a new test set of 40 known, random $\vec{S}_{true}$ was measured with the metasurface polarimeter, and the $\vec{S}_{measured}$ were reconstructed. The rmse error on the test set was 3.00%, which is only marginally larger than for the calibration set. A selection of eight reconstructed $\vec{S}_{measured}$, including the mesurements with the highes and lowest error, are shown overlaid on the $\vec{S}_{true}$, with the rms error for each test $\vec{S}$, in Figure S10.

The error monitoring feature of the original design is demonstrated here, with each combination of four orders out of (-4,-3,-2,+1,+4) having an adequately low rms error on $\vec{S}$ reconstruction. Figure S11 shows the inverse condition numbers for each combination of 4-measurements (a) and the corresponding rms error for the combination of 4-measurements (b) for the set test of 40 $\vec{S}$, with the total rms error stemming from factors additional to those attributed to the polarisation performance calculated from the condition number. The 4-measurement reconstructions that had the highest rms errors were the sets that removed the -4 and +4 analyser orders respectively (labelled as '1' and '5' in Figure S11). The error associated with removing any of the analyser orders is a complex interaction between the diattenuation, efficiency, and analyser vector of that order. +4 is, for example, one of the best performing orders for diattenuation, but has a lower efficiency, and is in relatively close proximity to the -3 analyser order (refer back to Figure S7(c)). The -4 order, comparatively, has a lower diattenuation,

higher efficiency, but is much more separated in proximity to the other analyser orders on the Poincaré sphere. Figure S12 shows the distribution of rms for each $\vec{S}$ for each combination of 4-measurement reconstructions. The worst performing combinations, number 1 and 5 have just over 10% as the maximum rms errors, which we consider to be the maximum level of acceptable error.

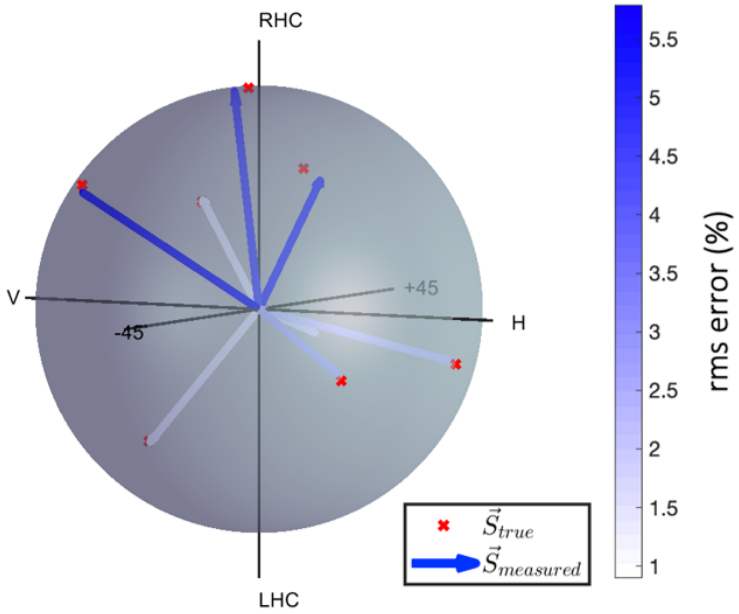

Figure S10: $\vec{S}_{true}$ (red crosses) and $\vec{S}_{measured}$ (vectors) for a selection of 8 states from the set of 40 random test states, including the measurements with the highest and lowest error. The rms error between $\vec{S}_{true}$ and $\vec{S}_{measured}$ is given by the colour of the $\vec{S}_{measured}$ vector.

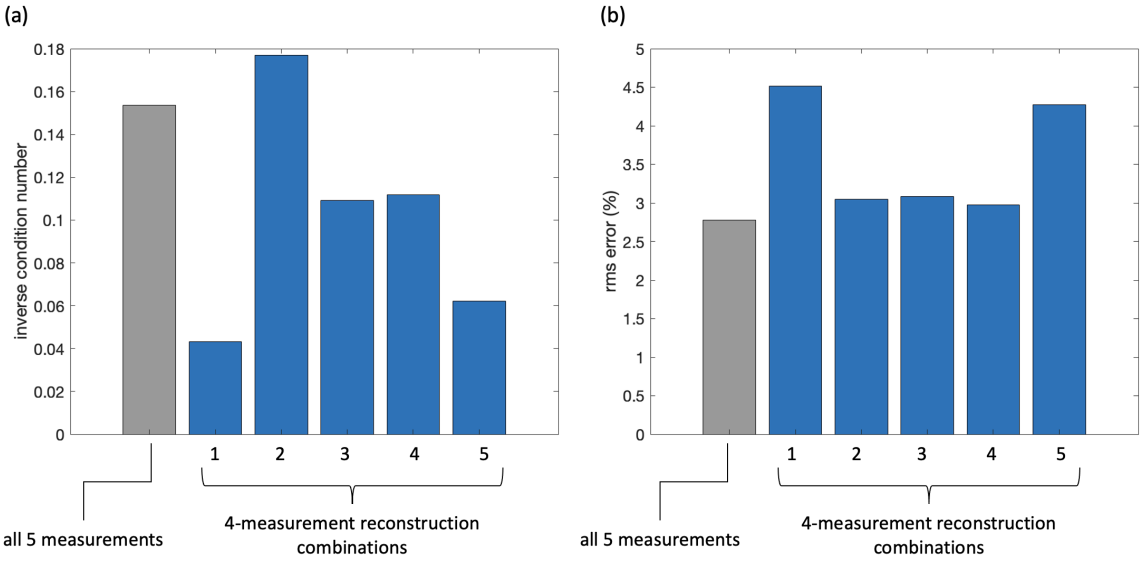

Figure S11: (a) Inverse condition numbers for five measurements and each combination of 4-measurements. The 5-measurement inverse condition number is the same as in Figure S7(c). (b) RMS error for 5 measurements and the combinations of 4-measurement for the set test of 40 $\vec{S}$.

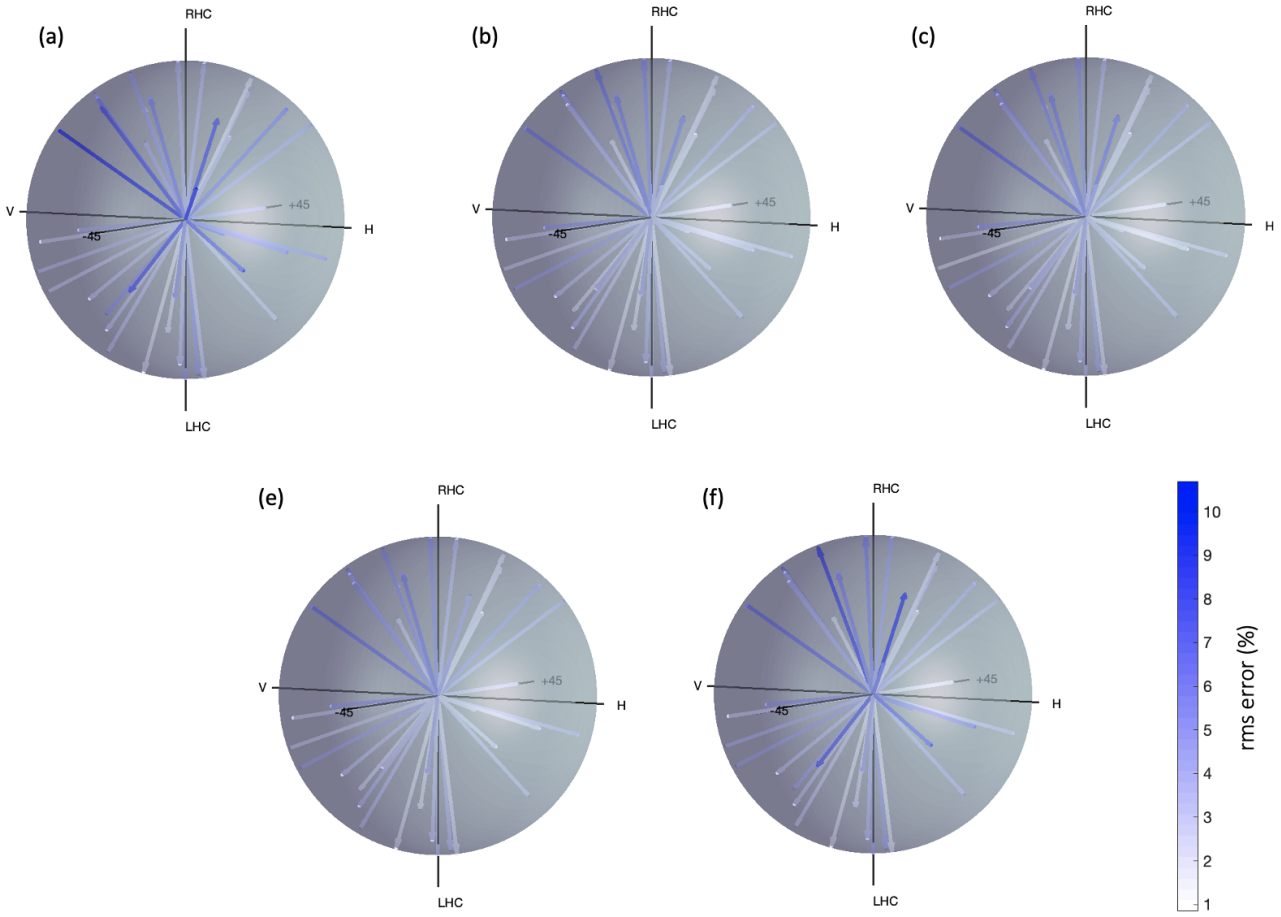

Figure S12: RMS error for each of the 4-measurement reconstruction combinations. (a), (b), (c), (d), (e), (f) correspond respectively to the 1, 2, 3, 4, 5 numbering given in Figure S11.

Bibliography

[S1] M. A. Green, *Self-consistent optical parameters of intrinsic silicon at 300K including temperature coefficients*, Solar Energy Materials and Solar Cells **92**(11), 1305–1310 (2008), doi:10.1016/j.solmat.2008.06.009.

[S2] S. Lung, K. Wang, N. R. H. Pedersen, F. Setzpfandt, and A. A. Sukhorukov, *Robust Classical and Quantum Polarimetry with a Single Nanostructured Metagrating*, ACS Photonics **11**(3), 1060–1067 (2024), doi:10.1021/acsphotonics.3c01287.

[S3] J. C. Suárez-Bermejo, J. C. G. de Sande, M. Santarsiero, and G. Piquero, *Analysis of the Errors in Polarimetry with Full Poincarè Beams*, in: 2019 PhotonIcs & Electromagnetics Research Symposium - Spring (PIERS-Spring), (2019), pp. 2621–2627, doi:10.1109/PIERS-Spring46901.2019.9017429.

[S4] J. Li, H. Liu, Y. Zheng, J. Lei, Q. Zhao, Z. Xiong, R. Liao, and H. Ma, *Accurate and robust calibration method for simultaneous Stokes polarimetry*, Measurement **223**, 113773 (2023), doi:10.1016/j.measurement.2023.113773.